Available online at www.sciencedirect.com
ScienceDirect
Comput. Methods Appl. Mech. Engrg. 196 (2006) 235–246
Computer methods in applied mechanics and engineering
www.elsevier.com/locate/cma

Hypersingular BEM for dynamic fracture in 2-D piezoelectric solids

A. Sáez [a,*], F. García-Sánchez [b], J. Domínguez [a]

[a] Departamento de Mecánica de Medios Continuos, Escuela Superior de Ingenieros, Universidad de Sevilla, Camino de los Descubrimientos s/n, 41092 Sevilla, Spain

[b] Departamento de Ingeniería Civil, E.T.S. de Ingenieros Industriales, Universidad de Málaga, Campus de El Ejido s/n, 29013 Málaga, Spain

Received 15 November 2005; received in revised form 16 February 2006; accepted 20 March 2006

Abstract

Fracture behavior of piezoelectric solids under time-harmonic loading is numerically analyzed in this paper. A 2-D boundary element method (BEM) based on both displacement and traction boundary integral equations is presented. The time-harmonic Green's functions for the infinite plane are split into singular plus regular terms, the singular ones coinciding with the static Green's functions. In this manner the singular and hypersingular integrals arising in the formulation may be treated by the same simple regularization procedure proposed by the authors for static piezoelectricity. Quarter-point elements are used for the direct evaluation of stress and electric displacement intensity factors from nodal values. Several numerical examples for the scattering of waves by different crack configurations including branched and curved cracks and crack interaction problems are given to demonstrate the performance of the proposed method.

Keywords: BEM; Piezoelectric solids; Dynamic fracture mechanics; Curved crack; Wave scattering

1. Introduction

In recent years structural control applications using piezoelectric materials are receiving increasing attention. Due to the inherent coupling between their electric and mechanical behavior, piezoelectric materials are being widely used as the actuator materials for active vibration control in smart structures. However, because of their brittleness piezoelectric materials have a tendency to develop cracks during their manufacturing process and service. The existence of such flaws critically affects the mechanical integrity and electromechanical behavior of these materials. Thus, the proper understanding and evaluation of the fracture process in piezoelectric materials are crucial to the advancement of modern intelligent material systems. As a consequence, this topic has attracted increasing attention from many researchers [2,3,11,12,14,19–21,26].

Analytical solutions are mostly restricted to simple geometries and load conditions, so that numerical methods are necessary for general complex applications. It is well known that the BEM presents significant advantages over other numerical techniques for the analysis of fracture mechanics problems [5]. In particular, only the boundary of the domain has to be discretized and very accurate results are obtained on the boundary. In the case of crack propagation, the advantage of the BEM are even more obvious since any remeshing process is fairly simple to achieve. Additionally when dealing with boundless regions under dynamic loading the radiation conditions at infinity are automatically satisfied, so only the internal boundaries need to be discretized. This fact has led to the publication of several BE approaches for the analysis of cracks in piezoelectric solids in the last few years. However, few papers on BE formulations for dynamic fracture of piezoelectric solids have been published. The main difficulties in the field are related to derivation and integration of fundamental solutions. Previous works by Pan [13] reported a single domain BEM formulation for 2-D static crack problems.

* Corresponding author. Tel.: +34 954487293; fax: +34 954487295.
E-mail addresses: andres@us.es (A. Sáez), fgsanchez@uma.es (F. García-Sánchez), jose@us.es (J. Domínguez).

0045-7825/$ - see front matter
doi:10.1016/j.cma.2006.03.002

He computed the hypersingular integrals using a numerical quadrature. A time-harmonic classical BEM formulation has recently been presented and implemented for straight line elements by Denda et al. [4]. Zhang and coworkers [23–25] have presented BEM formulations to study crack problems in the time domain subjected to both anti-plane and in-plane loading.

In this paper we investigate the response of cracked 2-D piezoelectric materials under time-harmonic dynamic loading by means of a hypersingular BEM approach. The time-harmonic fundamental solution obtained by Denda et al. [4] is split into singular and regular parts, the singular one coinciding with the static fundamental solution. In this manner, only regular (frequency dependent) terms need to be added to the static BEM formulation previously developed by García-Sánchez et al. [8] in order to solve the dynamic problem. The generality of this procedure permits the use of general straight or curved quadratic boundary elements. In particular, discontinuous quarter-point elements are used to capture the crack-tip behavior. Stress (SIF) and electric displacement (EDIF) intensity factors are computed directly from nodal values of the crack opening displacements (COD) and the electric potential jump at the quarter-point element.

As compared to Ref. [4], the present paper includes the hypersingular and the mixed formulations for dynamic crack piezoelectric problems. The procedure allows to represent cracks by means of quadratic straight or curved crack elements. Denda et al. [4] presented the basic classical BEM formulation and its use was restricted to straight elements to solve general eigenvalue problems.

Several numerical examples are presented to illustrate the accuracy and robustness of the present approach. In particular, kinked and curved crack geometries as well as interaction between cracks subjected to mechanical in-plane loading are presented for the first time. These obtained results may be considered as benchmark results for future research.

2. A frequency domain mixed BEM formulation for dynamic fracture in piezoelectric materials

A mixed or dual BEM formulation for crack problem is next presented. Pioneer dual BEM formulations were developed by Chen, Aliabadi and co-workers [1,10,18] for isotropic and anisotropic media.

The mixed BEM formulation presented herein is an extension of the one previously developed by the authors for anisotropic crack problems [9]. This may be easily achieved provided that piezoelectric materials are always anisotropic and their behavior can be formulated in an elastic-like fashion, as in Barnett and Lothe [2], by using a displacement vector extended with the electric potential (φ)

$$u_I = \begin{cases} u_i & I = 1,2, \\ \varphi & I = 3 \end{cases} \tag{1}$$

and a stress tensor extended with the electric displacement components (D_i)

$$\sigma_{iJ} = \begin{cases} \sigma_{ij} & J = 1,2, \\ D_i & J = 3. \end{cases} \tag{2}$$

These extended stresses will have an associated tractions vector extended with the normal electric displacement (D)

$$p_I = \begin{cases} p_i = \sum_{j=1}^{2} \sigma_{ij} n_j & I = 1,2, \\ D = \sum_{j=1}^{2} D_j n_j & I = 3. \end{cases} \tag{3}$$

The constitutive relations may be written as

$$\sigma_{iJ} = C_{iJLm} u_{L,m}, \tag{4}$$

where the lowercase (elastic) and uppercase (extended) subscripts take values 1, 2 and 1, 2, 3; respectively.

In Eq. (4) the behavior matrix, C_{iJKl}, contains the elastic moduli C_{ijkl}, the piezoelectric coefficients, e_{ijk} and the dielectric constants, ε_{ij}; according to the following expression

$$C_{iJKl} = \begin{cases} C_{ijkl} & J,K = 1,2, \\ e_{lij} & J = 1,2;\ K = 3, \\ e_{ikl} & J = 3;\ K = 1,2, \\ -\varepsilon_{il} & J,K = 3. \end{cases} \tag{5}$$

The mixed formulation of the BEM for Fracture Mechanics applications makes use of both the extended displacement and the traction integral representations. The 2-D displacement integral representation for a collocation point $\boldsymbol{\xi}$ in an piezoelectric domain Ω with boundary Γ can be written for time-harmonic loading as

$$c_{IJ}(\boldsymbol{\xi}) u_J(\boldsymbol{\xi},\omega) + \int_\Gamma p^*_{IJ}(\boldsymbol{x},\boldsymbol{\xi},\omega) u_J(\boldsymbol{x},\omega)\, \mathrm{d}\Gamma(\boldsymbol{x}) = \int_\Gamma u^*_{IJ}(\boldsymbol{x},\boldsymbol{\xi},\omega) p_J(\boldsymbol{x},\omega)\, \mathrm{d}\Gamma(\boldsymbol{x}), \tag{6}$$

where $I,J = 1,2,3$; $\boldsymbol{x}$ is an observation point on the boundary Γ; ω is the angular frequency of excitation; u^*_{IJ} and p^*_{IJ} are the fundamental solution displacements and tractions, respectively; and $c_{IJ}(\boldsymbol{\xi})$ is the so-called free term that results from the Cauchy principal value (CPV) integration of the strongly singular p^*_{IJ} kernels.

The 2-D hypersingular traction integral representation for the same source point $\boldsymbol{\xi}$ can be obtained by differentiation of Eq. (6) with respect to ξ_k and the subsequent application of Hooke's law, to yield

$$c_{IJ}(\boldsymbol{\xi}) p_J(\boldsymbol{\xi},\omega) + N_r \int_\Gamma s^*_{rIJ}(\boldsymbol{x},\boldsymbol{\xi},\omega) u_J(\boldsymbol{x},\omega)\, \mathrm{d}\Gamma(\boldsymbol{x}) = N_r \int_\Gamma d^*_{rIJ}(\boldsymbol{x},\boldsymbol{\xi},\omega) p_J(\boldsymbol{x},\omega)\, \mathrm{d}\Gamma(\boldsymbol{x}), \tag{7}$$

where $r = 1,2$ and $\mathbf{N}$ denotes the outward unit normal to the boundary at the source point.

The kernels s^*_{rIJ} and d^*_{rIJ} are, therefore, obtained by differentiation of p^*_{IJ} and u^*_{IJ}, respectively, with the following expressions

$$d^*_{rIJ} = C_{rIMl} u^*_{MJ,l}, \tag{8}$$

$$s^*_{rIJ} = C_{rIMl} p^*_{MJ,l}. \tag{9}$$

Let $\Gamma = \Gamma_C \cup \Gamma_{crack}$, $\Gamma_{crack} = \Gamma_+ \cup \Gamma_-$ being the two geometrically coincident crack lines and Γ_C denoting the rest of the (crack free) boundary. To solve crack problems, the traction boundary integral equation (BIE) will be applied on either side of the crack, say Γ_+, and the displacement BIE on Γ_C to yield a complete set of equations to compute the extended displacements and tractions on Γ_C and the extended crack opening displacements (ECOD) on Γ_{crack}

$$c_{IJ} u_J + \int_{\Gamma_C} p^*_{IJ} u_J \, d\Gamma + \int_{\Gamma_+} p^*_{IJ} \Delta u_J \, d\Gamma = \int_{\Gamma_C} u^*_{IJ} p_J \, d\Gamma, \tag{10}$$

$$p_I + N_r \int_{\Gamma_C} s^*_{rIJ} u_J \, d\Gamma + N_r \int_{\Gamma_+} s^*_{rIJ} \Delta u_J \, d\Gamma = N_r \int_{\Gamma_C} d^*_{rIJ} p_J \, d\Gamma, \tag{11}$$

where the independent variables have been omitted for the sake of clarity.

Note that in Eq. (11) the free term has been set to 1 because of the additional singularity arising from the coincidence of the two crack surfaces.

To write Eqs. (10) and (11) the cracks considered are free of tractions or self-equilibrated from the mechanical point of view, and subjected to impermeable conditions from the electrical point of view, so that

$$\Delta p = p^+_K + p^-_K = 0, \tag{12}$$

where the superscripts + and − stand for the upper and lower crack surfaces, respectively.

Computation of the traction BIE requires C^1 continuity of the displacements. As in previous works [6–9] discontinuous quadratic elements with the two extreme collocation nodes shifted towards the element interior are used to mesh the cracks. The asymptotic ECOD behavior near the tip of the crack is captured by means of discontinuous quarter-point elements (see Fig. 1). Semidiscontinuous elements are used on the external boundaries when intersection with a crack occurs. For the rest of the boundaries, continuous quadratic elements are employed. A complete justification of the discretization procedure may be found in [7,8].

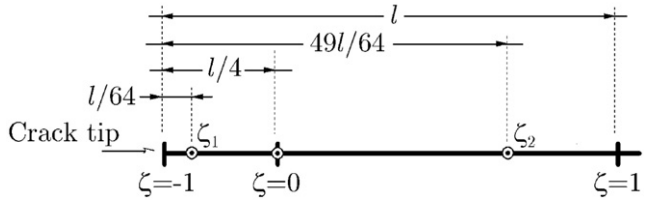

Fig. 1. Discontinuous quarter point element (for $\zeta_1 = -0.75$ and $\zeta_2 = +0.75$).

3. Fundamental solutions

Green's functions for 2-D piezoelectric elastic media under time-harmonic loading have been obtained by Denda et al. [4], based on the Radon transform. They follow a similar procedure to that proposed by Wang and Achenbach [22] for anisotropic solids.

The fundamental solution displacements are then given in the form of a contour integral over a unit circumference as

$$u^*_{IJ}(\boldsymbol{x}, \boldsymbol{\xi}, \omega) = \frac{1}{8\pi^2} \int_{|\boldsymbol{\eta}|=1} \sum_{m=1}^{2} \frac{\mathscr{E}^m_{IJ}(\boldsymbol{\eta})}{\rho c^2_m(\boldsymbol{\eta})} \Psi(k_m |\boldsymbol{\eta} \cdot (\boldsymbol{x} - \boldsymbol{\xi})|) \, dS(\boldsymbol{\eta}), \tag{13}$$

where $\boldsymbol{\eta} = (\eta_1, \eta_2)$ is a unit vector describing the position on the unit circumference; c_m are the phase velocities; $k_m = \omega / c_m$ are the wave numbers; ρ is the density of the material and

$$\mathscr{E}^m_{IJ}(\boldsymbol{\eta}) = \begin{cases} E^m_{ij}(\boldsymbol{\eta}) / E^m_{kk}(\boldsymbol{\eta}) & I, J = 1, 2 \\ -\dfrac{E^m_{iq}(\boldsymbol{\eta}) \Gamma_{q3}(\boldsymbol{\eta})}{\Gamma_{33}(\boldsymbol{\eta}) E^m_{kk}(\boldsymbol{\eta})} & I = 1, 2; \; J = 3 \\ \dfrac{E^m_{pq}(\boldsymbol{\eta}) \Gamma_{3p}(\boldsymbol{\eta}) \Gamma_{q3}(\boldsymbol{\eta})}{\Gamma^2_{33}(\boldsymbol{\eta}) E^m_{kk}(\boldsymbol{\eta})} & I = J = 3 \end{cases} \quad \text{(Sum on } k\text{)} \tag{14}$$

where Γ_{IJ} is the Christoffel matrix defined as

$$\Gamma_{IJ}(\boldsymbol{\eta}) = C_{rIJs} \eta_r \eta_s \tag{15}$$

and $E^m_{jk}(\boldsymbol{\eta})$ is given by

$$E^m_{jk}(\boldsymbol{\eta}) = \mathrm{adj}(\widehat{\Gamma}_{jk}(\boldsymbol{\eta}) - \delta_{jk} \lambda_m(\boldsymbol{\eta})), \tag{16}$$

where $\widehat{\Gamma}_{ij}$ is the reduced Christoffel matrix

$$\widehat{\Gamma}_{ij}(\boldsymbol{\eta}) = \Gamma_{ij}(\boldsymbol{\eta}) - \frac{\Gamma_{i3}(\boldsymbol{\eta}) \Gamma_{3j}(\boldsymbol{\eta})}{\Gamma_{33}(\boldsymbol{\eta})} \tag{17}$$

and $\lambda_m(\boldsymbol{\eta})$ are the eigenvalues of $\widehat{\Gamma}_{ij}$.

The $\Psi(s)$ function in Eq. (13) is defined as

$$\Psi(s) = i\pi \exp(is) - 2[\cos(s)\,\mathrm{ci}(s) + \sin(s)\,\mathrm{si}(s)], \tag{18}$$

$\mathrm{ci}(s)$ and $\mathrm{si}(s)$ being the cosine and sine integrals

$$\mathrm{ci}(s) = -\int_s^\infty \frac{\cos(t)}{t} dt = \gamma + \int_0^s \frac{\cos(t) - 1}{t} dt + \ln(s), \tag{19}$$

$$\mathrm{si}(s) = -\int_s^\infty \frac{\sin(t)}{t} dt. \tag{20}$$

Green's functions in Eq. (13) may be decomposed into the sum of singular plus regular terms as shown in [4]

$$u^*_{IJ}(\boldsymbol{x}, \boldsymbol{\xi}, \omega) = u^{*S}_{IJ}(\boldsymbol{x}, \boldsymbol{\xi}) + u^{*R}_{IJ}(\boldsymbol{x}, \boldsymbol{\xi}, \omega). \tag{21}$$

The singular part is frequency independent and it coincides with the piezoelectric elastostatic Green's functions

$$u^{*S}_{IJ}(\boldsymbol{x}, \boldsymbol{\xi}) = \frac{-1}{4\pi^2} \int_{|\boldsymbol{\eta}|=1} \sum_{m=1}^{2} \frac{\mathscr{E}^m_{IJ}(\boldsymbol{\eta})}{\rho c^2_m(\boldsymbol{\eta})} \log |\boldsymbol{\eta} \cdot (\boldsymbol{x} - \boldsymbol{\xi})| \, dS(\boldsymbol{\eta}), \tag{22}$$

whilst the regular part is frequency dependent

$$u^{*R}_{IJ}(\boldsymbol{x},\boldsymbol{\xi},\omega)=\frac{1}{8\pi^2}\int_{|\boldsymbol{\eta}|=1}\sum_{m=1}^{2}\frac{\mathscr{E}^m_{IJ}(\boldsymbol{\eta})}{\rho c_m^2(\boldsymbol{\eta})}\Psi^R(k_m,|\boldsymbol{\eta}\cdot(\boldsymbol{x}-\boldsymbol{\xi})|)\,\mathrm{d}S(\boldsymbol{\eta}), \tag{23}$$

where

$$\Psi^R(k_m,|\boldsymbol{\eta}\cdot(\boldsymbol{x}-\boldsymbol{\xi})|)=\Psi(k_m|\boldsymbol{\eta}\cdot(\boldsymbol{x}-\boldsymbol{\xi})|)+2\log|\boldsymbol{\eta}\cdot(\boldsymbol{x}-\boldsymbol{\xi})|. \tag{24}$$

The corresponding fundamental solution tractions are obtained for the regular part as

$$\begin{aligned}p^{*R}_{IJ}(\boldsymbol{x},\boldsymbol{\xi},\omega)&=C_{mJRl}u^{*R}_{IR,l}(\boldsymbol{x},\boldsymbol{\xi},\omega)n_m\\&=\frac{1}{8\pi^2}\int_{|\boldsymbol{\eta}|=1}\sum_{m=1}^{2}\frac{\mathscr{E}^m_{IR}(\boldsymbol{\eta})}{\rho c_m^2(\boldsymbol{\eta})}\overline{\Gamma}_{JR}k_m\psi\\&\quad\times(k_m|\boldsymbol{\eta}\cdot(\boldsymbol{x}-\boldsymbol{\xi})|)\mathrm{sign}[\boldsymbol{\eta}\cdot(\boldsymbol{x}-\boldsymbol{\xi})]\,\mathrm{d}S(\boldsymbol{\eta}),\end{aligned} \tag{25}$$

where

$$\overline{\Gamma}_{JR}=C_{mJRl}n_m\eta_l \tag{26}$$

and

$$\psi(k_m|\boldsymbol{\eta}\cdot(\boldsymbol{x}-\boldsymbol{\xi})|)=\frac{\partial\Psi^R(k_m,|\boldsymbol{\eta}\cdot(\boldsymbol{x}-\boldsymbol{\xi})|)}{\partial x_l}, \tag{27}$$

so that

$$\psi(s)=-\pi\exp(\mathrm{i}s)-2[\cos(s)\,\mathrm{si}(s)-\sin(s)\,\mathrm{ci}(s)]. \tag{28}$$

For the sake of simplicity and numerical efficiency the explicit static piezoelectric fundamental solution obtained using the complex variable solution approach, as in García-Sánchez et al. [8], will be considered

$$u^{*S}_{IJ}(\boldsymbol{x},\boldsymbol{\xi})=-\frac{1}{\pi}\mathrm{Re}\left\{\sum_{M=1}^{3}A_{JM}H_{MI}\ln\left(z^x_M-z^\xi_M\right)\right\}, \tag{29}$$

where z^ξ and z^x are, respectively, the source and the observation point defined on the complex plane from their coordinates on the real plane as

$$z^\xi_M=\xi_1+\mu_M\xi_2;\quad z^x_M=x_1+\mu_M x_2;\qquad M=1,2,3, \tag{30}$$

μ_M being the roots of the following characteristic equation

$$|C_{1lJ1}+(C_{1lJ2}+C_{2lJ1})\mu_M+C_{2lJ2}\mu_M^2|=0. \tag{31}$$

The roots of (31) are either complex or purely imaginary and always occur in conjugate pairs [2]. For each of these characteristic roots μ_M, the columns of the $\mathbf{A}$ matrix are obtained from

$$[C_{1lJ1}+(C_{1lJ2}+C_{2lJ1})\mu_M+C_{2lJ2}\mu_M^2]A_{JM}=0\quad(\text{no sum on } M) \tag{32}$$

and the matrix $\mathbf{H}$ is obtained from

$$\mathbf{H}=\mathbf{A}^{-1}(\mathbf{B}^{-1}+\overline{\mathbf{B}}^{-1})^{-1}\quad\text{with }\mathbf{B}=\mathrm{i}\mathbf{A}\mathbf{L}^{-1}, \tag{33}$$

where the components of the $\mathbf{L}$ matrix are given by

$$\begin{aligned}L_{IM}&=\sum_{R=1}^{3}[C_{2IR1}+C_{2IR2}\mu_M]A_{RM}\\&=-\frac{1}{\mu_M}\sum_{R=1}^{3}[C_{1IR1}+C_{1IR2}\mu_M]A_{RM}\\&\quad(\text{no sum on } M).\end{aligned} \tag{34}$$

From Eq. (29) follow the static fundamental solution tractions as

$$p^{*S}_{IJ}(\boldsymbol{x},\boldsymbol{\xi})=-\frac{C_{rJKn}}{\pi}\mathrm{Re}\left\{\sum_{M=1}^{3}A_{KM}H_{MI}\frac{z^x_{M,n}}{z^x_M-z^\xi_M}\right\}n_r, \tag{35}$$

where

$$z^x_{M,n}=\frac{\partial z^x_M}{\partial x_n}=\delta_{1n}+\mu_M\delta_{2n};\quad n=1,2;\ M=1,2,3. \tag{36}$$

Using the expression (34), Eq. (35) may be rewritten as

$$p^{*S}_{ij}(\boldsymbol{x},\boldsymbol{\xi})=\frac{1}{\pi}\mathrm{Re}\left\{\sum_{m=1}^{2}L_{jm}H_{mi}\frac{\mu_m n_1-n_2}{z^x_m-z^\xi_m}\right\}. \tag{37}$$

The roots μ_M and the matrices $\mathbf{A}$ and $\mathbf{L}$ may be computed alternatively by solving the following eigenvalue problem [2]

$$\boldsymbol{\Xi}\boldsymbol{\vartheta}_\alpha=\mu_\alpha\boldsymbol{\vartheta}_\alpha, \tag{38}$$

where

$$\boldsymbol{\Xi}=\begin{pmatrix}-C^{-1}_{2lJ2}C_{2lJ1} & -C^{-1}_{2lJ2}\\ -C_{1lJ2}C^{-1}_{2lJ2}C_{2lJ1}+C_{1lJ1} & -C_{1lJ2}C^{-1}_{2lJ2}\end{pmatrix} \tag{39}$$

and

$$\boldsymbol{\vartheta}_\alpha=\begin{pmatrix}\mathbf{A}_\alpha\\ \mathbf{B}_\alpha\end{pmatrix}. \tag{40}$$

The elastostatic Green's functions defined in Eqs. (22) and (29) only differ by the constant terms $\varkappa_{IJ}$ (see Ref. [4] for details)

$$\varkappa_{IJ}=\frac{1}{\pi}\mathrm{Re}\left\{\sum_{M=1}^{3}A_{JM}H_{MI}\ln(\mathrm{i}-\mu_M)\right\};\quad(\mathrm{i}=\sqrt{-1}). \tag{41}$$

These constants are inessential for the elastostatic BEM formulation [4], but they are required for the time-harmonic BEM.

The derivatives of the fundamental solution displacements at the collocation point are evaluated from

$$u^{*S}_{MJ,l}(\boldsymbol{x},\boldsymbol{\xi})=\frac{\partial u^{*S}_{MJ}(\boldsymbol{x},\boldsymbol{\xi})}{\partial\xi_l}=\frac{1}{\pi}\mathrm{Re}\left\{\sum_{R=1}^{3}A_{JR}H_{RM}\frac{z^\xi_{R,l}}{z^x_R-z^\xi_R}\right\} \tag{42}$$

for the displacements singular part and

$$\begin{aligned}u^{*R}_{MJ,l}(\boldsymbol{x},\boldsymbol{\xi},\omega)&=-\frac{1}{8\pi^2}\int_{|\boldsymbol{\eta}|=1}\sum_{q=1}^{2}\frac{\mathscr{E}^q_{MJ}(\boldsymbol{\eta})}{\rho c_q^2(\boldsymbol{\eta})}k_q\eta_l\psi\\&\quad\times(k_q|\boldsymbol{\eta}\cdot(\boldsymbol{x}-\boldsymbol{\xi})|)\mathrm{sign}(\boldsymbol{\eta}\cdot(\boldsymbol{x}-\boldsymbol{\xi}))\,\mathrm{d}S(\boldsymbol{\eta})\end{aligned} \tag{43}$$

for the displacements regular part.

Similarly, the derivatives of the fundamental solution tractions at the collocation point are obtained as

$$p^{*S}_{MJ,l}(\boldsymbol{x},\boldsymbol{\xi}) = \frac{1}{\pi}\mathrm{Re}\left\{\sum_{R=1}^{3} L_{JR}H_{RM}\frac{\mu_R n_1 - n_2}{(z^x_R - z^\xi_R)^2}z^\xi_{R,l}\right\} \tag{44}$$

for the singular part of the solution and as

$$p^{*R}_{MJ,l}(\boldsymbol{x},\boldsymbol{\xi},\omega) = \frac{1}{8\pi^2}\int_{|\boldsymbol{\eta}|=1}\sum_{q=1}^{2}\frac{\mathscr{E}^q_{MR}(\boldsymbol{\eta})}{\rho c_q^2(\boldsymbol{\eta})}\overline{\Gamma}_{JR}k_q^2\eta_l\Psi \times (k_q|\boldsymbol{\eta}\cdot(\boldsymbol{x}-\boldsymbol{\xi})|)\,\mathrm{d}S(\boldsymbol{\eta}) \tag{45}$$

for the regular part, where $\Psi(s)$ has been previously defined in Eq. (18).

4. Integration scheme and implementation

To compute the integrals of the fundamental solution singular part, the same kind of singular and hypersingular integrations that arise in the elastostatic mixed BEM formulation for piezoelectrics need to be solved. We here follow the regularization procedure developed by García-Sánchez et al. [8] for static crack analysis. Therefore, all the singular and hypersingular integrals are transformed into regular integrals and simple singular integrals with known analytical solution. A brief description of this procedure is given in the appendix for completeness.

Once the static problem has been dealt with, only regular (frequency dependent) terms need to be added to the static BEM formulation in order to solve the dynamic problem. The computation of the integrals associated to the regular part involve a double numerical integration: first along the unit circumference $|\boldsymbol{\eta}| = 1$ and then over the boundary element. In the case of the s^{*R}-kernels terms in (11), the integration is done numerically with a logarithmic quadrature that accounts for the weak singularity shown by the tractions derivatives. Alternatively, in Denda et al. [4], straight elements are considered for the displacement BIE, and the order of integration is exchanged provided that the dynamic terms are regular. Then, the integration over the boundary element is done analytically, leaving only the line integral over the unit circumference for numerical evaluation.

The generality of the present approach permits the use of general straight or curved quadratic boundary elements. In particular, discontinuous quarter-point elements are used to capture the $\sqrt{r}$ displacement behavior near the crack tips, r being the distance to the tip [12,19,21].

For fracture applications, the SIF and EDIF need to be computed. To do so, only the leading terms of the extended displacement field around the tip need to be considered in the crack tip vicinity. The following relation between the crack opening displacements and the electrical potential jumps across the crack, and the SIF and EDIF, respectively, holds

$$\begin{pmatrix} K_{\mathrm{II}} \\ K_{\mathrm{I}} \\ K_{\mathrm{IV}} \end{pmatrix} = \sqrt{\frac{\pi}{8\bar{r}}}\mathbf{Q}^{-1}\begin{pmatrix} \Delta u_1 \\ \Delta u_2 \\ \Delta\varphi \end{pmatrix}, \tag{46}$$

$\bar{r}$ being the distance between the crack tip and the point where Δu_1, Δu_2 and $\Delta\varphi$ are evaluated and

$$\mathbf{Q} = \mathrm{Re}(\mathbf{B}), \tag{47}$$

where $\mathbf{B}$ has been previously defined in Eq. (33).

The performance of the straight discontinuous quarter-point element used in the present work (Fig. 1) has been widely tested in preceding works [15,6,8,9] for both static and dynamic applications in isotropic and anisotropic materials. It has a collocation point very close to the crack tip, so that direct substitution of the nodal values of the ECOD at this point ($\bar{r} = l/64$, l being the quarter-point element length) into Eq. (46) provides an accurate and robust procedure to determine the intensity factors with little mesh dependence.

5. Numerical examples

Scattering of time-harmonic waves impinging on cracks embedded in different infinite plane piezoelectric media are analysed in this section.

To validate the proposed approach a straight crack is first considered and the obtained results are favorably compared with the semi-analytical solution given by Shindo and Ozawa [16] and Shindo et al. [17].

Once the method is validated, results for branched cracks, curved cracks and interaction between parallel and collinear cracks are presented for the first time in the literature.

5.1. Incident time-harmonic waves

The analysis of wave scattering by cracks in infinite media is done by superposition of two problems. One, the incident field in the uncracked domain, and the other, the cracked domain loaded on the crack faces by tractions equal and opposite to those appearing in the uncracked domain along the crack line. Since there are not infinite values of the stress in the uncracked plane, the SIF and EDIF in the original diffraction problem are the same as in the second problem (scattered field).

The piezoelectric plane solids considered for all the following examples show a poling axis that coincides with the x_2 axis, so that the matrix that governs their constitutive law has the form

$$\begin{pmatrix} C_{11} & C_{12} & 0 & 0 & e_{21} \\ C_{12} & C_{22} & 0 & 0 & e_{22} \\ 0 & 0 & C_{66} & e_{16} & 0 \\ 0 & 0 & e_{16} & -\varepsilon_{11} & 0 \\ e_{21} & e_{22} & 0 & 0 & -\varepsilon_{22} \end{pmatrix}. \tag{48}$$

Both P and SV incident waves are considered:

5.1.1. Incident P-wave

The incident wave motion is characterized by the following extended displacement components

$$u_1 = 0; \quad u_2 = \hat{u}_2 \exp[\mathrm{i}\omega(x_2/c_p + t)];$$
$$\varphi = \hat{\varphi} \exp[\mathrm{i}\omega(x_2/c_p + t)] \tag{49}$$

with associated extended stress tensor components given by

$$\begin{aligned}
\sigma_{11} &= \mathrm{i}\omega/c_p(C_{12}\hat{u}_2 + e_{21}\hat{\varphi}) \exp[\mathrm{i}\omega(x_2/c_p)],\\
\sigma_{22} &= \mathrm{i}\omega/c_p(C_{22}\hat{u}_2 + e_{22}\hat{\varphi}) \exp[\mathrm{i}\omega(x_2/c_p)],\\
\sigma_{12} &= 0,\\
D_{11} &= 0,\\
D_{22} &= \mathrm{i}\omega/c_p(e_{22}\hat{u}_2 - \varepsilon_{22}\hat{\varphi}) \exp[\mathrm{i}\omega(x_2/c_p)].
\end{aligned} \tag{50}$$

The extended tractions for a surface with outer normal components n_1, n_2 will be given as

$$\begin{aligned}
p_1 &= \frac{\varepsilon_{22}C_{12} + e_{12}e_{22}}{\varepsilon_{22}C_{22} + e_{22}^2} n_1\sigma_0 \exp[\mathrm{i}\omega(x_2/c_p)],\\
p_2 &= n_2\sigma_0 \exp[\mathrm{i}\omega(x_2/c_p)],\\
D_n &= 0.
\end{aligned} \tag{51}$$

5.1.2. Incident SV-wave

For this case, the extended displacements are

$$u_1 = \hat{u}_1 \exp[\mathrm{i}\omega(x_2/c_s + t)]; \quad u_2 = 0; \quad \varphi = 0 \tag{52}$$

with extended stress tensor components

$$\begin{aligned}
\sigma_{11} &= 0,\\
\sigma_{22} &= 0,\\
\sigma_{12} &= \tau_0 \exp[\mathrm{i}\omega(x_2/c_s)],\\
D_{11} &= \tau_0 \frac{e_{16}}{C_{66}} \exp[\mathrm{i}\omega(x_2/c_s)],\\
D_{22} &= 0
\end{aligned} \tag{53}$$

and an extended tractions vector

$$\begin{aligned}
p_1 &= n_2\tau_0 \exp[\mathrm{i}\omega(x_2/c_s)],\\
p_2 &= n_1\tau_0 \exp[\mathrm{i}\omega(x_2/c_s)],\\
D_n &= \frac{e_{16}}{C_{66}} n_1\tau_0 \exp[\mathrm{i}\omega(x_2/c_s)].
\end{aligned} \tag{54}$$

In Eqs. (49)–(54), the symbol "^" stands for the amplitude of a magnitude, $c_p = \sqrt{(C_{22} + e_{22}^2/\varepsilon_{22})/\rho}$, $c_s = \sqrt{C_{66}/\rho}$, ρ being the density of the material, $\sigma_0 = \mathrm{i}\omega\hat{u}_2(C_{22} + e_{22}^2/\varepsilon_{22})/c_p$ and $\tau_0 = \mathrm{i}\omega\hat{u}_1/c_s$.

5.2. Straight crack

First the problem of a crack normal to the poling axis has been analysed when the incident motion is a P-wave traveling along this axis. Plane strain conditions are assumed. Three different piezoelectric materials have been considered: PZT–6B, PZT–5H and $BaTiO_3$, whose properties are given in Table 1.

Table 1
Properties of materials considered in the examples

	C_{11}	C_{22}	C_{66}	C_{12}	e_{21}	e_{22}	e_{16}	ε_{11}	ε_{22}
PZT-4	139	74.3	113	25.6	−6.98	13.84	13.44	6	5.47
PZT-5H	126	117	23	84.1	−6.5	23.3	17.0	15.04	13
PZT-6B	168	163	27.1	60	−0.9	7.1	4.6	3.6	3.4
$BaTiO_3$	150	146	44	66	−4.35	17.5	11.4	9.87	11.2

Units: C_{ij} (MPa), e_{ij} (C/m^2), ϵ_{ij} (C/(GV m)).

The BE mesh consists of 10 elements with lengths decreasing uniformly towards the crack tips, so that the length-ratio between the central and crack tip elements is two. This same mesh is used for the rest of the examples involving straight cracks.

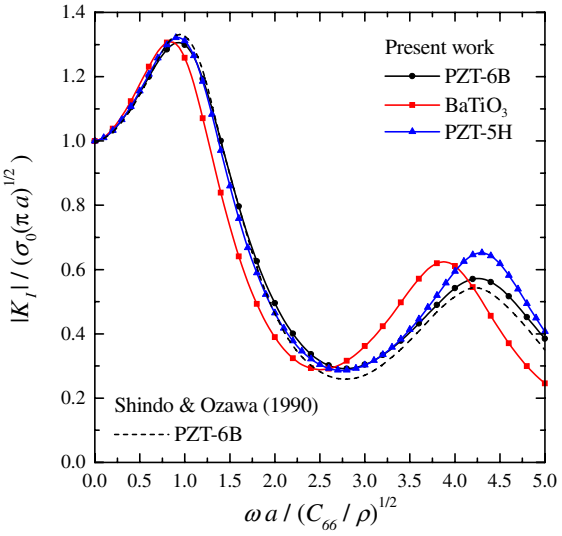

Fig. 2. Normalized K_{I} versus dimensionless frequency. Straight crack, P-wave impinging normally.

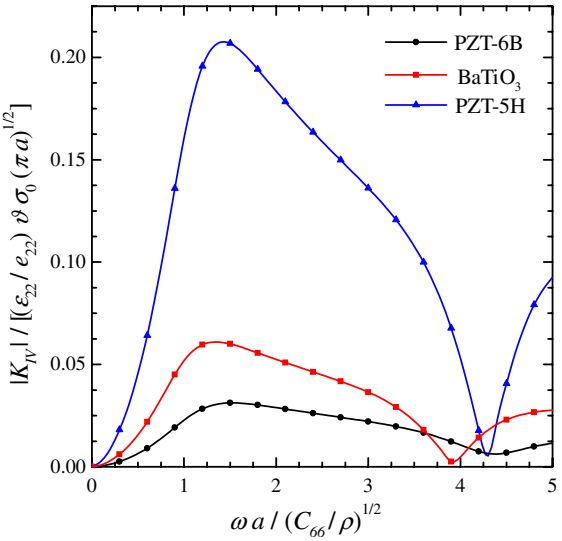

Fig. 3. Normalized K_{IV} versus dimensionless frequency. Straight crack, P-wave impinging normally.

Fig. 2 shows the obtained normalized SIF for mode I versus the dimensionless frequency $\omega a/c_s$, together with the previous results presented for PZT–6B, by Shindo and Ozawa [16] by means of a semi-analytical method. In Fig. 3 the normalized EDIF is plotted versus the dimensionless frequency.

Next, the FFT is used to obtain results for the transitory response of the straight crack to an impact load applied normally to the crack (see Fig. 4). The results for mode I SIF versus time are compared with the ones published by Shindo et al. [17] in Fig. 5. Due to the problem symmetries mode II SIF is null. Fig. 6 shows the results for the transitory EDIF.

In all the cases good agreement with Shindo et al. [16,17] solutions is observed. Results in Fig. 2 show a difference below 2% for the peak value of the SIF. Results in Fig. 5 show slightly larger differences between both sets of solutions for the time where the peak values of the SIF are reached. The discontinuity in the slope shown by the BEM results is of the same type of that obtained by analytical procedures for elastic crack problems [5], and it is a consequence of the arrival of the Rayleigh waves diffracted by the other tip.

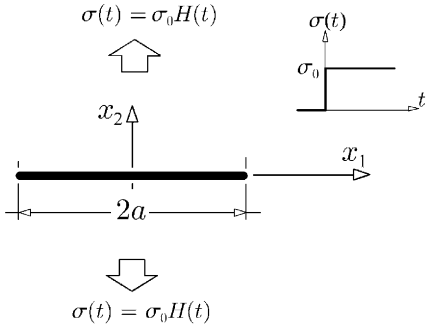

Fig. 4. Straight crack under impact load.

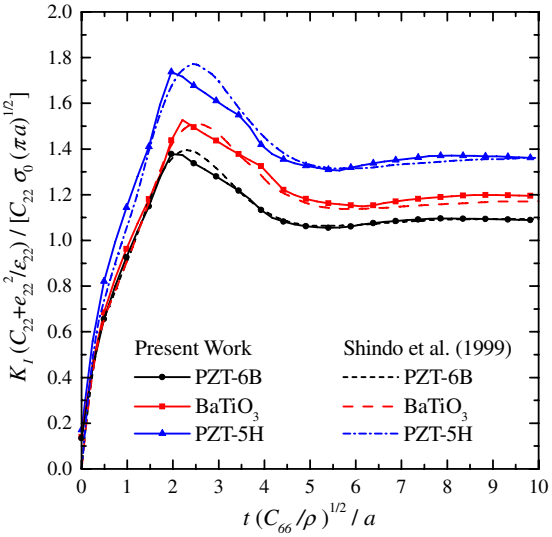

Fig. 5. Normalized K_I versus dimensionless time. Straight crack under impact load.

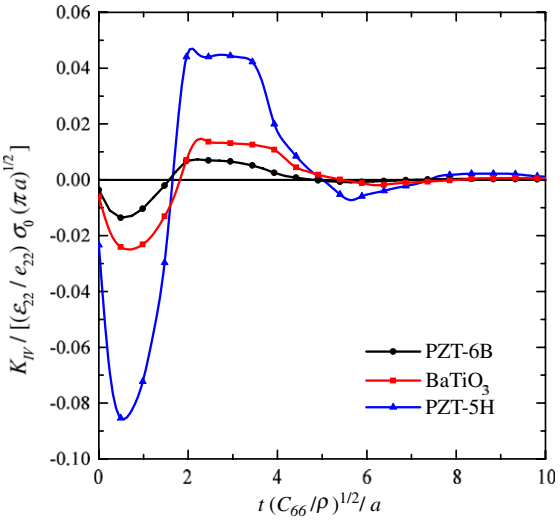

Fig. 6. Normalized K_{IV} versus dimensionless time. Straight crack under impact load.

5.3. Parallel cracks

In the following example the problem of two parallel cracks of equal length under normal impinging P-waves is considered (see Fig. 7). The cracks are oriented

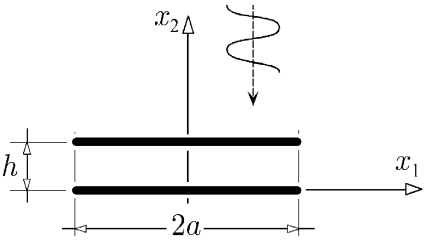

Fig. 7. Parallel cracks under P-wave impinging normally.

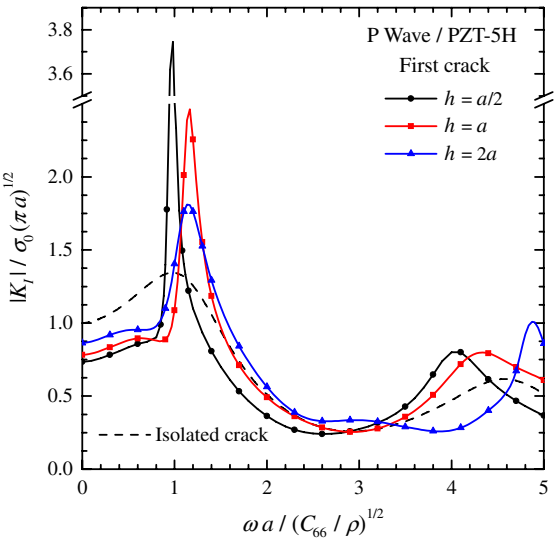

Fig. 8. Normalized K_I at upper crack versus dimensionless frequency. Parallel cracks under normal P-wave.

perpendicular to the poling axis of the piezoelectric PZT–5H material. Results are presented for different separation between cracks. Plain stress conditions are assumed.

For the sake of brevity only results for the upper crack are shown. Results for the lower crack can be found in Ref. [7]. The results for the case of an isolated straight crack have been included in the graphics as a reference to illustrate the effect of the second crack on the SIF and EDIF behavior.

Fig. 8 shows the normalized SIF for mode I versus the dimensionless frequency $\omega a/c_s$. As it could be expected the peak values are higher as the distance between the cracks decreases. Such peak values are obtained for values of the dimensionless frequency around 1, and are above the peak value observed for an isolated crack.

Fig. 9 illustrates the appearance of mode II SIF as a consequence of the existence of a second crack, with significant peak values as the distance between the cracks decreases.

Fig. 10 shows the normalized EDIF plotted versus the dimensionless frequency.

5.4. Collinear cracks

Next, the case of two equal length collinear straight cracks is analysed. The cracks are located normally to the poling axis of the PZT–5H material and are subjected to an incident P-wave impinging normally onto the cracks (Fig. 11). Once more, results are obtained for different values of the separation between cracks.

In Figs. 12 and 13 mode I SIF and EDIF are plotted, respectively, versus frequency. The interaction between cracks is far less significant than for the previous example. In particular there is not mode II SIF, as for the isolated crack case. The results shown correspond to the external tip of the cracks. Results for the internal tips may be found in Ref. [7].

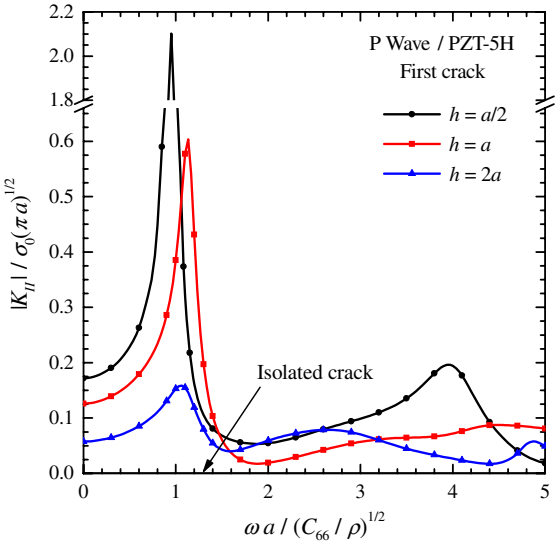

Fig. 9. Normalized K_{II} at upper crack versus dimensionless frequency. Parallel cracks under normal P-wave.

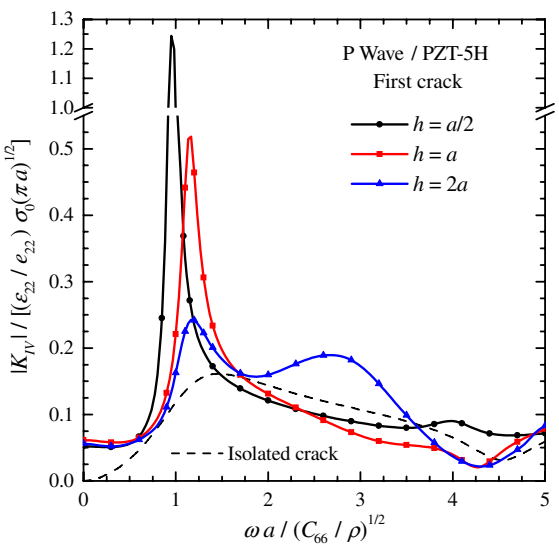

Fig. 10. Normalized K_{IV} at upper crack versus dimensionless frequency. Parallel cracks under normal P-wave.

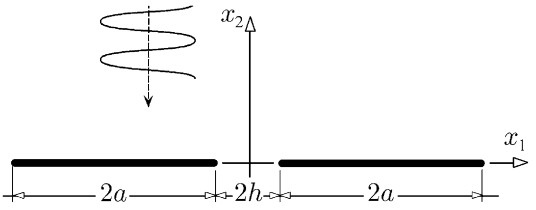

Fig. 11. Collinear cracks under normal P-wave.

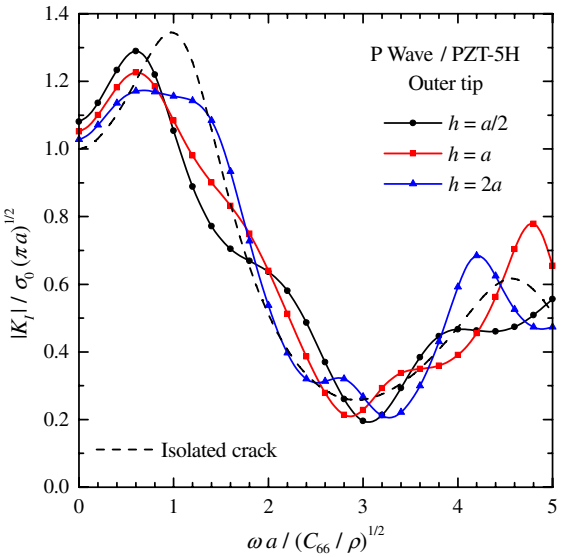

Fig. 12. Normalized K_I at outer tip versus dimensionless frequency. Collinear cracks under normal P-wave.

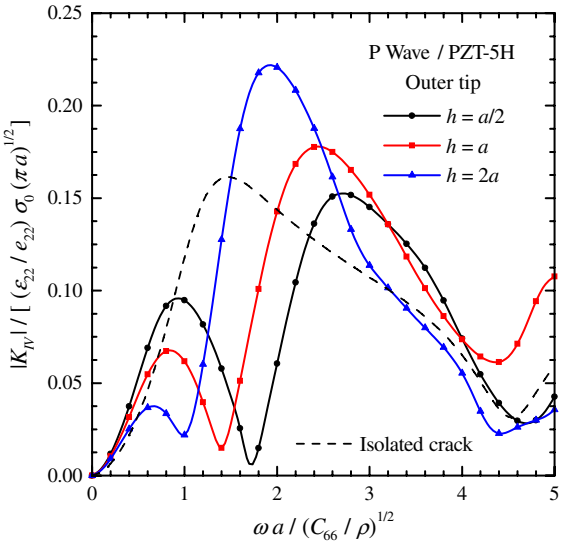

Fig. 13. Normalized K_{IV} at outer tip versus dimensionless frequency. Collinear cracks under normal P-wave.

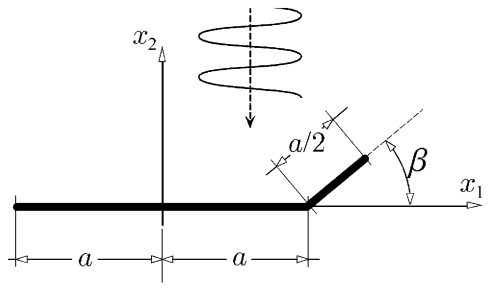

Fig. 14. Branched cracks under SV-wave impinging normally onto the mother crack.

5.5. Branched crack

A mother–daughter crack problem subjected to a SV-wave impinging normally onto the mother crack, is analysed next (Fig. 14). The piezoelectric material considered is a PZT-4. Both branches form an angle β between them, so that for positive β angles the branch tip is reached by the incident wave before the main crack. Results for an incident P-wave can be consulted in Ref. [7].

The BE mesh consists of ten elements with decreasing size to the crack tips for the main crack and five elements for the crack branch with increasing size to the mid-length of the branch.

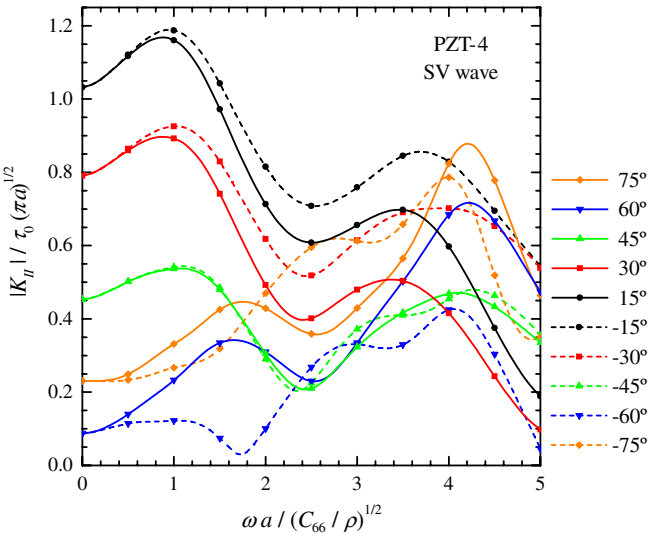

Fig. 16. Normalized K_{II} at branch tip versus dimensionless frequency for different branch angles. Branched crack under normal SV-wave.

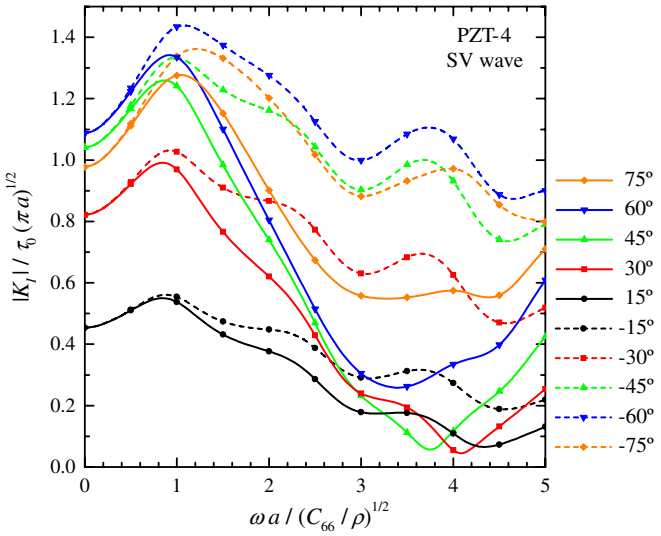

Fig. 15. Normalized K_I at branch tip versus dimensionless frequency for different branch angles. Branched crack under normal SV-wave.

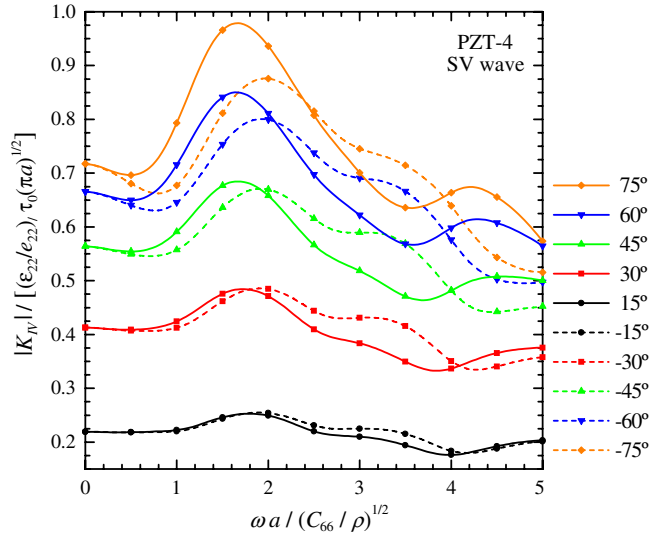

Fig. 17. Normalized K_{IV} at branch tip versus dimensionless frequency for different branch angles. Branched crack under normal SV-wave.

Fig. 15 illustrates how the mode I SIF K_I increases with the angle between branches. Nevertheless this tendency inverts for large angles, as it can be observed for $\beta = 75°$. The main difference between the results obtained for positive and negative values of β is found after the first peak value, given rise to a substantially larger decrease for positive than for negative β angles.

Results for mode II SIF are plotted in Fig. 16. The greater values correspond now to smaller branch angles, as it could be expected. In this case, the influence of the angle sign is significantly more important for the larger angles.

Results obtained for the EDIF are shown in Fig. 17. Such values increase with the angle between branches for the whole range analysed. This intensity factor is less sensitive to the frequency than K_I and K_{II}.

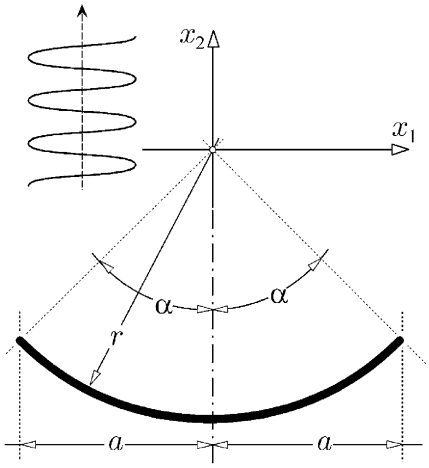

Fig. 18. Circular arch crack under SV-wave impinging normally to the chord.

5.6. Curved crack

Finally, a circular arch crack in a PZT–4 subjected to an incident SV-wave impinging along the material poling axis, and normally to the arch chord, is considered. The arch shape is defined by the semi-angle α (see Fig. 18).

The crack is discretized into 10 elements. The ones at the tips are very small (arch length/30) quarter-point straight elements whilst the rest are curved quadratic discontinuous boundary elements.

The results presented are the mode I and II SIF (Figs. 19 and 20) and the EDIF (Fig. 21) versus frequency for several

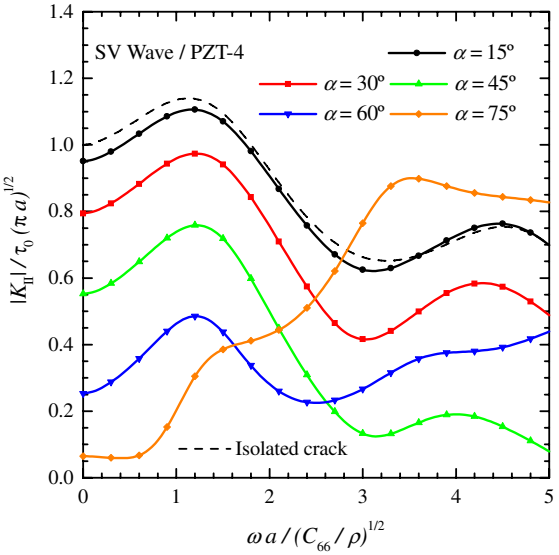

Fig. 20. Normalized K_{II} versus dimensionless frequency. Circular arch crack defined by the semiangle α under a SV-wave impinging normally to the chord.

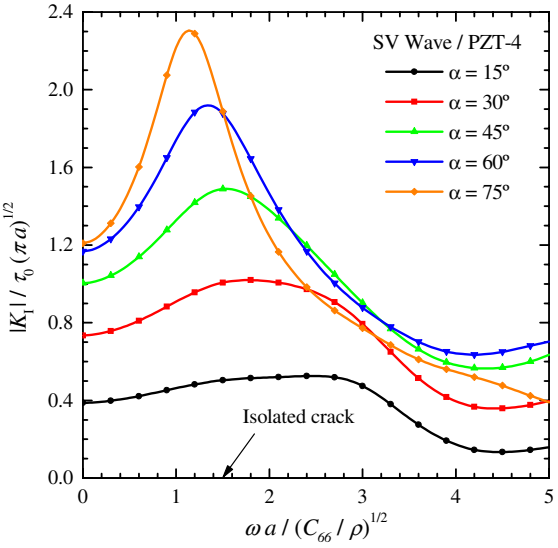

Fig. 19. Normalized K_I versus dimensionless frequency. Circular arch crack defined by the semiangle α under a SV-wave impinging normally to the chord.

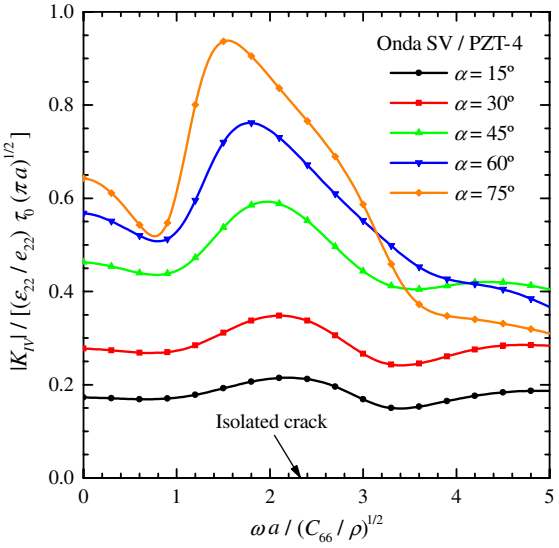

Fig. 21. Normalized K_{IV} versus dimensionless frequency. Circular arch crack defined by the semiangle α under a SV-wave impinging normally to the chord.

values of the arch angle α. Results for an isolated straight crack have been included in the figures to illustrate the effect of crack curvature.

The case of an incident P-wave as well as some other additional results involving different geometries and loads may be found in [7].

6. Conclusions

A mixed BEM approach for the solution of time-harmonic two-dimensional fracture problems in piezoelectric solids has been presented. The time-harmonic Green's functions derived by Denda et al. [4] are divided into singular static plus regular frequency dependent parts. In this way the singular and hypersingular integrals that arise from the singular part of the fundamental solution can be dealt with as in the elastostatic case [8]. Subsequently the regular part is added up in order to solve the dynamic problem.

This method requires no numerical integration of strongly singular nor hypersingular integrals thanks to an easy-to-implement regularization procedure. This allows for an accurate evaluation of the SIF and EDIF for any crack geometry with rather coarse meshes, provided that discontinuous quarter-point elements are adopted to model the $\sqrt{r}$ displacement behavior near the crack tips.

The accuracy and robustness of the present BEM approach has been demonstrated by comparison of the obtained results with some published solutions for a straight crack. Several other examples including kinked and curved crack geometries as well as interaction between cracks have been presented for the first time.

Acknowledgments

This work was supported by the Ministerio de Ciencia y Tecnología of Spain (DPI2004-08147-C02-02). The financial support is gratefully acknowledged.

Appendix A. Regularization of singular and hypersingular integrals

For the sake of completeness, a brief description of the integration procedure developed by the authors [8] for static piezoelectricity in next given.

After discretization of the boundaries and the field variables, integrals of the p^*-kernels lead to basic singular integrals of order $\mathrm{O}[1/(z_R^x - z_R^\xi)]$ when the source point belongs to the integration element Γ_e as

$$I_p = \int_{\Gamma_e} \frac{\mu_R n_1 - n_2}{z_R^x - z_R^\xi} \phi_q \, \mathrm{d}\Gamma \quad (\text{no sum on } R), \tag{A.1}$$

where ϕ_q are the boundary element shape functions.

Similarly, integrals of the d^*-kernels lead to basic singular integrals of order $\mathrm{O}[1/(z_R^x - z_R^\xi)]$ as

$$I_d = \int_{\Gamma_e} \frac{\mu_R N_1 - N_2}{z_R^x - z_R^\xi} \phi_q \, \mathrm{d}\Gamma \quad (\text{no sum on } R), \tag{A.2}$$

whilst integrals of the s^*-kernels lead to basic hypersingular integrals of order $\mathrm{O}[1/(z_R^x - z_R^\xi)^2]$ as

$$I_s = \int_{\Gamma_e} \frac{\mu_R n_1 - n_2}{(z_R^x - z_R^\xi)^2} \phi_q \, \mathrm{d}\Gamma. \tag{A.3}$$

Considering the change of variables

$$\chi_R = z_R - z_R^\xi = (x_1 - \xi_1) + \mu_R (x_2 - \xi_2), \tag{A.4}$$

it follows that the jacobian of the transformation that maps the boundary onto the complex plane has the expression (see Fig. 22)

$$\frac{\mathrm{d}\chi_R}{\mathrm{d}\Gamma} = \frac{\mathrm{d}\chi_R}{\mathrm{d}x_1}\frac{\mathrm{d}x_1}{\mathrm{d}\Gamma} + \frac{\mathrm{d}\chi_R}{\mathrm{d}x_2}\frac{\mathrm{d}x_2}{\mathrm{d}\Gamma} = -n_2 + \mu_R n_1. \tag{A.5}$$

Taking into account Eqs. (A.4) and (A.5), I_p can be transformed to yield

$$\begin{aligned} I_p &= \int_{\Gamma_e} \frac{1}{\chi_R} \phi_q \, \mathrm{d}\chi_R \\ &= \int_{\Gamma_e} \frac{1}{\chi_R} (\phi - 1) \, \mathrm{d}\chi_R + \int_{\Gamma_e} \frac{1}{\chi_R} \, \mathrm{d}\chi_R, \end{aligned} \tag{A.6}$$

where the first integral is regular and can be computed using a standard Gauss quadrature while the second one has a well known analytical solution.

Similarly, I_d can be transformed to yield

$$\begin{aligned} I_d &= \int_{\Gamma_e} \frac{(\mu_R N_1 - N_2 \pm \mathrm{d}\chi_R/\mathrm{d}\Gamma)}{\chi_R} \phi_q \, \mathrm{d}\Gamma \\ &= \int_{\Gamma_e} \frac{(\mu_R N_1 - N_2 - \mathrm{d}\chi_R/\mathrm{d}\Gamma)}{\chi_R} \phi_q \, \mathrm{d}\Gamma \\ &\quad + \int_{\Gamma_e} \frac{1}{\chi_R} \phi_q \, \mathrm{d}\chi_R, \end{aligned} \tag{A.7}$$

where the first of the integrals is regular since $\mathrm{d}\chi_R/\mathrm{d}\Gamma \to (\mu_R N_1 - N_2)$ as $\boldsymbol{x} \to \boldsymbol{\xi}$. The second integral coincides with I_p and its computation has been described before.

Finally, I_s can be transformed with the help of Eqs. (A.4) and (A.5) as

$$I_s = \int_{\Gamma_e} \frac{1}{\chi_R^2} \phi \, \mathrm{d}\chi_R. \tag{A.8}$$

This integral is regularized by means of the Taylor series expansion of the shape function, ϕ_q, considered as a function of the complex χ_R variable, i.e.,

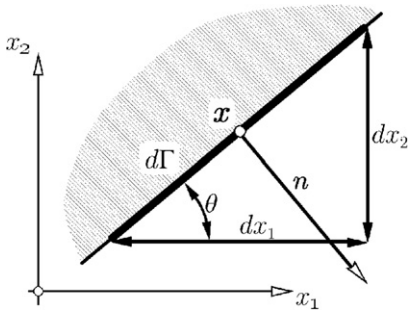

Fig. 22. Differential boundary element and outward normal at collocation point.

$$\phi(\chi_R \approx 0) = \phi(\chi_R = 0) + \left.\frac{\mathrm{d}\phi}{\mathrm{d}\chi_R}\right|_{\chi_R=0} \chi_R + \mathrm{O}(\chi_R^2) = \phi_0 + \phi_0'\chi_R + \mathrm{O}(\chi_R^2) \tag{A.9}$$

to yield

$$I_s = \int_{\Gamma_e} \frac{1}{\chi_R^2}(\phi \pm (\phi_0 + \phi_0'\chi_R))\,\mathrm{d}\chi_R = \int_{\Gamma_e} \frac{\phi - (\phi_0 + \phi_0'\chi_R)}{\chi_R^2}\mathrm{d}\chi_R + \phi_0 \int_{\Gamma_e} \frac{1}{\chi_R^2}\mathrm{d}\chi_R + \phi_0' \int_{\Gamma_e} \frac{1}{\chi_R}\mathrm{d}\chi_R, \tag{A.10}$$

where the first integral is regular and the rest of integrals are singular and hypersingular, respectively, but having well known analytical solutions.

References

[1] E.L. Albuquerque, P. Sollero, M.H. Aliabadi, Dual boundary element method for anisotropic dynamic fracture mechanics, Int. J. Numer. Methods Engrg. 59 (2004) 1187–1205.

[2] D.M. Barnett, J. Lothe, Dislocations and line charges in anisotropic piezoelectric insulators, Phys. State Solid (b) 76 (1975) 105–111.

[3] W.F. Deeg, The analysis of dislocation, crack and inclusion problems in piezoelectric solids, Ph.D. thesis, Stanford University, 1980.

[4] M. Denda, Y. Araki, Y.K. Yong, Time-harmonic BEM for 2-D piezoelectricity applied to eigenvalue problems, Int. J. Solids Struct. 41 (26) (2004) 7241–7265.

[5] J. Domínguez, Boundary Elements in Dynamics, Computational Mechanics Publications, Southampton & Elsevier Applied Science, London, 1993.

[6] F. García, A. Sáez, J. Domínguez, Traction boundary elements for cracks in anisotropic solids, Engrg. Anal. Bound. Elem. 28 (2004) 667–676.

[7] F. García-Sánchez, Numerical study of fracture problems in anisotropic elastic and piezoelectric solids, Ph.D. thesis, University of Sevilla, Spain, 2005.

[8] F. García-Sánchez, A. Sáez, J. Domínguez, Anisotropic and piezoelectric materials fracture analysis by BEM, Comput. Struct. 83 (2005) 804–820.

[9] F. García-Sánchez, A. Sáez, J. Domínguez, Two-dimensional time-harmonic BEM for cracked anisotropic solids, Engrg. Anal. Bound. Elem. 30 (2006) 88–99.

[10] H.-K. Hong, J.-T. Chen, Derivations of integral equations of elasticity, J. Engrg. Mech. ASCE 114 (1988) 1028–1044.

[11] X.-F. Li, K.Y. Lee, Fracture analysis of cracked piezoelectric materials, Int. J. Solids Struct. 41 (2004) 4137–4161.

[12] Y.E. Pak, Linear electro-elastic fracture mechanics of piezoelectric materials, Int. J. Fract. 54 (1992) 79–100.

[13] E. Pan, A BEM analysis of fracture mechanics in 2D anisotropic piezoelectric solids, Engrg. Anal. Bound. Elem. 23 (1999) 67–76.

[14] S.B. Park, C.T. Sun, Fracture criteria for piezoelectric ceramics, J. Am. Ceram. Soc. 78 (1995) 1475–1480.

[15] A. Sáez, R. Gallego, J. Domínguez, Hypersingular quarter-point boundary elements for crack problems, Int. J. Numer. Methods Engrg. 38 (1995) 1681–1701.

[16] Y. Shindo, E. Ozawa, Dynamic analysis of a cracked piezoelectric material, in: R.K.T. Hsieh (Ed.), Mechanical Modelling of New Electromagnetic Materials, Elsevier, 1990, pp. 297–304.

[17] Y. Shindo, F. Narita, E. Ozawa, Impact response of a finite crack in an orthotropic piezoelectric ceramic, Acta Mech. 137 (1999) 99–107.

[18] P. Sollero, M.H. Aliabadi, Anisotropic analysis of cracks in composite laminates using the dual boundary element method, Comput. Struct. 31 (1995) 229–233.

[19] H. Sosa, On fracture mechanics of piezoelectric solids, Int. J. Solids Struct. 29 (1992) 2613–2622.

[20] H. Sosa, N. Khutoryansky, New developments concerning piezoelectric materials with defects, Int. J. Solids Struct. 33 (1996) 3399–3414.

[21] Z. Suo, C.-M. Kuo, D.M. Barnett, J.R. Willis, Fracture mechanics for piezoelectric ceramics, J. Mech. Phys. Solids 4 (1992) 739–765.

[22] C.-Y. Wang, J.D. Achenbach, Elastodynamic fundamental solutions for anisotropic solids, Geophys. J. Int. 118 (1994) 384–392.

[23] C.-Y. Wang, Ch. Zhang, 3-D and 2-D Dynamic Green's functions and time-domain BIEs for piezoelectric solids, Engrg. Anal. Bound. Elem. 29 (5) (2005) 454–465.

[24] Ch. Zhang, Transient dynamic analysis of cracked piezoelectric solids by a time-domain BIEM, in: H.A. Mang, F.G. Rammerstorfer, J. Eberhardsteiner (Eds.), Proceedings of the Fifth World Congress on Computational Mechanics (WCCMV), Vienna University of Technology, Vienna, Austria, 7–12 July 2002, ISBN 3-9501554-0-6.

[25] Ch. Zhang, C.-Y. Wang, S. Hirose, A time-domain BIEM for dynamic crack analysis of a piezoelectric solid, in: Z. Yao, M.H. Aliabadi (Eds.), Boundary Element Techniques, Tsinghua University Press, 2002, pp. 119–126.

[26] T.Y. Zhang, C.F. Gao, Fracture behaviors of piezoelectric materials, Theoret. Appl. Fract. Mech. 41 (2004) 339–379.